Journal of Materials Chemistry A

ROYAL SOCIETY OF CHEMISTRY

PAPER

View Article Online
View Journal | View Issue

Cite this: J. Mater. Chem. A, 2025, 13, 24727

A comparative electrochemical study of 2H/1T phases of MoS_2 and designing 1T-MoS_2@Cu_2S for high-performance supercapacitors†

Arkapriya Das,[a] Alakananda Paul,[a] Ankita Mondal,[a] Kaushik Pal [bc] and Bhanu Bhusan Khatua *[a]

Received 20th May 2025
Accepted 24th June 2025

DOI: 10.1039/d5ta04052c

rsc.li/materials-a

Two-dimensional materials, such as MoS_2, have recently attracted significant attention due to their excellent electrical properties, offering great potential for sustainable energy storage solutions through supercapacitor applications. In this study, we conduct a comparative investigation of the supercapacitor performance of two phases of MoS_2, namely the semiconducting 2H phase and the metallic 1T phase. Additionally, we employed two distinct and complementary synthesis approaches, namely exfoliation and hydrothermal synthesis, to determine the most effective strategy for enhancing supercapacitor performance. Our results show that the 1T phase synthesized *via* the hydrothermal method exhibits superior supercapacitor performance. Nevertheless, the intrinsic limitations of MoS_2, including its low density of active edge sites and inert basal plane, hinder its electrochemical activity. To address these challenges, Cu_2S was strategically incorporated into the 1T phase of MoS_2, forming a hierarchical composite with snowflake-like morphology and a dendritic structure. This architecture promotes efficient ion transport and ensures a seamless electrode–electrolyte interface. Moreover, the composite facilitates a synergistic charge transfer network between MoS_2 and Cu_2S by leveraging the metallic nature of the 1T phase, achieving a high specific capacitance of 1118 F g^{-1} at 1 A g^{-1}. When paired with MnO_2 in an asymmetric hybrid device, it delivers an impressive energy density of 141 Wh kg^{-1} and a power density of 19 000 W kg^{-1}, highlighting its promise for next-generation energy storage systems.

Introduction

Supercapacitors are an active research area due to their remarkable properties, such as high-power density, fast charge–discharge capability, and long operational lifespan, offering distinct advantages over conventional batteries and capacitors.[1] Several research efforts have focused on developing advanced electrode materials, transition metal oxides,[2,3] metal nitrides,[4] transition metal chalcogenides,[5,6] layered two-dimensional (2D) materials[7,8] and hybrid nanostructures,[9,10] each known for high electrical conductivity, rich electrochemical activity, and tunable structural properties. Within this group, layered metal chalcogenides (*e.g.* MoS_2 (ref. 11 and 12), WS_2 (ref. 13 and 14), and TiS_2 (ref. 15 and 16)) with their 2D morphology have gained significant attention owing to their large surface area[17] for redox reaction active sites,[18] efficient ion transport,[19] and facile intercalation/deintercalation enabled by weak van der Waals interactions,[20] factors that collectively enhance both charge storage capacity and rate performance. Among these materials, MoS_2 stands out as a promising candidate for supercapacitor applications due to its structural similarity to graphene, featuring an interlayer spacing of 0.615 nm, significantly larger than graphite's 0.335 nm.[21] Its layered architecture allows chemical adaptability,[22] supporting diverse applications. MoS_2 exists in multiple polymorphs, primarily the semiconducting 2H phase and the metallic 1T phase.[23] To fabricate these distinct phases, various synthesis methods have been explored, including top-down approaches such as mechanical stripping,[24] liquid phase stripping or exfoliation,[25] and ion intercalation[26] and bottom-up techniques such as physical vapour deposition,[27] chemical vapour deposition,[28] and hydrothermal or solvothermal synthesis.[29] The 2H phase with trigonal prismatic coordination is thermodynamically stable[30] and widely studied for electronics though limited by poor conductivity and low cycling stability. In contrast, the 1T phase, featuring octahedral coordination, offers higher conductivity and superior charge storage, making it highly desirable for supercapacitor

[a]Materials Science Centre, Indian Institute of Technology Kharagpur, Kharagpur-721302, India. E-mail: khatuabb@matsc.iitkgp.ac.in; Tel: +91-3222 283982

[b]Centre for Nanotechnology, Indian Institute of Technology Roorkee, Roorkee, 247667, India

[c]Department of Mechanical and Industrial Engineering, Indian Institute of Technology Roorkee, Roorkee, 247667, India

† Electronic supplementary information (ESI) available: Materials and methods, useful equations for calculation of d spacing, Tauc plots, XRD spectra, FTIR graphs, BET curves, XPS spectra, UV-vis spectra, CV plots, GCD curves, Nyquist plot, and characterization of MnO_2. See DOI: https://doi.org/10.1039/d5ta04052c

electrodes.[31] However, a key challenge lies in stabilizing the 1T phase, as it tends to spontaneously revert to the more stable 2H phase over time due to its higher surface energy. As a result, careful selection of synthesis methods becomes critical for controlling the phase composition and achieving long-term stabilization of the 1T phase. While top-down approaches, including lithium intercalation-assisted exfoliation, often introduce defects and compromise structural integrity, bottom-up methods provide greater control over crystallinity and phase stabilization.[32] Additionally, integrating stabilizing agents into a composite structure presents an effective means of retaining the 1T phase, ensuring that its superior electrical conductivity can be fully exploited. An optimized bottom-up hydrothermal strategy enables 1T MoS_2-based composites by forming strong interfacial bonds and reducing surface energy *via* incorporation of a secondary metal sulfide. The main objective of this work is to uncover new insights into the limitations and enhancement of MoS_2-based systems by isolating both the effects of the phase and synthesis methods and then integrating the most promising elements into a single, advanced composite. In this work, we employed two complementary synthesis methods, exfoliation and hydrothermal synthesis, to fabricate both 2H and 1T phases of MoS_2 and compared their supercapacitor performance. Our results demonstrate that the 1T-MoS_2 material synthesized *via* the hydrothermal method outperformed its exfoliated counterpart. To further enhance structural stability and electrochemical performance, Cu_2S was incorporated into the 1T phase to form a MoS_2@Cu_2S composite. Cu_2S has gained significant attention for its applications in photocatalysis, sensing, switching devices, and energy storage and has been synthesized in diverse morphologies—including snowflake-like structures known for their high surface area and abundant active sites.[33] These architectures facilitate ion diffusion, prevent agglomeration of MoS_2 nanosheets, and improve charge storage. In addition, Cu_2S exhibits superior electrical conductivity,[34] redox activity[35] and an intrinsic synergistic effect when integrated with 1T-MoS_2. This synergistic effect addresses the key limitations of MoS_2-based supercapacitors, such as low specific capacitance and poor cycling stability[36] by maintaining the metallic nature of the 1T phase and significantly boosting electrochemical performance. Consequently, the 1T MoS_2@Cu_2S hybrid stands out as a highly promising candidate for next-generation energy storage applications. The optimized composite delivers a high specific capacitance of 1118 F g^{-1} at 1 A g^{-1}, excellent cycling stability with 95% retention over 15 000 cycles, and an impressive energy density of 141 Wh kg^{-1} with a power density of 19 000 W kg^{-1}. These findings contribute to the development of next-generation supercapacitors through effective phase engineering and hybrid composite design for sustainable energy storage.

Experimental section

Chemicals

Sodium molybdate dihydrate ($Na_2MoO_4 \cdot 2H_2O$), copper(II) chloride dihydrate ($CuCl_2 \cdot 2H_2O$), thiourea ($(NH_2)_2CS$), glacial acetic acid, ethylene diamine (EDA), nitric acid (HNO_3), potassium hydroxide (KOH), polyvinylidene fluoride (PVDF), *N*-methyl-2-pyrrolidinone (NMP), polyvinyl alcohol (PVA), acetone, Nafion, ethanol and propanol are procured from Merck, India. Chitosan is supplied by HiMedia Laboratories Pvt. Ltd, Mumbai, India. Bulk molybdenum disulphide (MoS_2) is obtained from RANKEM. Carbon black (99.9%) is purchased from Alfa Aesar. All the reagents are of analytical grade, *i.e.* trace purity is equal to or >95%. These can be used for any analytical applications that have severe quality specifications. They are used without any modification.

Top down method

Preparation of 2H-MoS_2 by exfoliation. Few sheets of 2H MoS_2 from the bulk 2H-MoS_2 powder were achieved by liquid phase exfoliation of the latter using chitosan as an intercalating agent. 30 mg of chitosan was dissolved in 15 mL of 4% (v/v) acetic acid solution after which 15 mg of bulk 2H-MoS_2 powder was added. The process involves the dispersion of bulk 2H-MoS_2 powder into chitosan solution using bath sonication for 30 min, followed by exfoliation of stacked MoS_2 sheets to nanosheets through probe sonication over a period of 4 h. The solution was centrifuged at 5000 rpm for 45 min to separate the unexfoliated or bulk 2H-MoS_2. The resulting supernatant undergoes further centrifugation at 8000 rpm for 45 min to collect the exfoliated MoS_2 nanosheets (termed ex-2H MoS_2) which are dried at room temperature for 48 h (Fig. 1a).

Bottom up approach

Preparation of 2H-MoS_2 by the hydrothermal method. 2H MoS_2 was synthesized by a one-step hydrothermal process. In a typical synthesis process, 0.125 M $Na_2MoO_4 \cdot 2H_2O$ as a Mo precursor and 0.65 M thiourea as a sulfur precursor were taken. The salts formed a homogeneous solution using DI water after vigorous stirring for 1 h. Finally, the mixture was transferred to a 100 mL Teflon-lined stainless steel autoclave and kept in a muffle furnace at 195 °C for 19 h. The black product was collected after centrifugation with DI water and with ethanol. The final product (named Hy-2H MoS_2) was kept in a hot air oven at 60 °C for 24 h (Fig. 1b).

Preparation of 1T MoS_2. 1T MoS_2 was also synthesized using the hydrothermal method. In this process 0.125 M $Na_2MoO_4 \cdot 2H_2O$ as a Mo precursor and 0.65 M thiourea as a sulfur precursor were taken. The solution was kept stirring for achieving homogeneity. To this solution, 85 μL HNO_3 and 5 mL ethanol were added and stirred well. Finally, the mixture was transferred to a 100 mL Teflon-lined stainless-steel autoclave and kept in a muffle furnace at 195 °C for 19 h. The black product was collected after centrifugation with DI water and with ethanol. The final product was kept in a hot air oven at 60 °C for 24 h. This product is assigned as hy-1T MoS_2. In this case, HNO_3 is used in order to facilitate the formation of the metastable 1T phase of MoS_2 by oxidizing Mo atoms slightly during the reaction, leading to the stabilization of the metallic 1T phase instead of the semiconducting 2H phase. It can also introduce defects in the MoS_2 layers, which are known to favour the stabilization of the 1T phase due to the increased energy

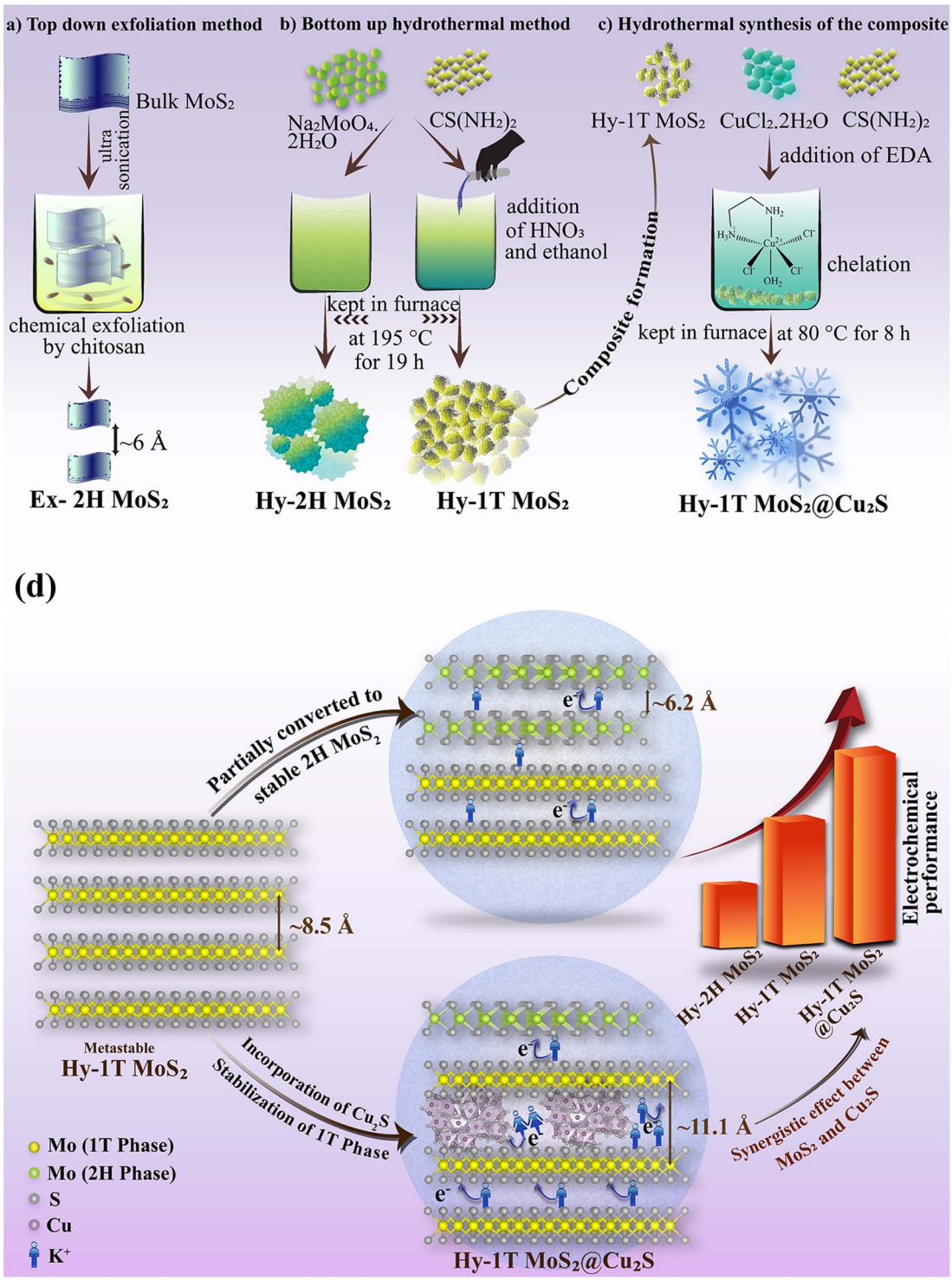

Fig. 1 Synthesis route for different phases of MoS_2, (a) top down method, (b) bottom up hydrothermal method, (c) hydrothermal method for preparation of the composite and (d) schematic representation describing the inherent stabilization process of the composite hy-1T MoS_2@Cu_2S towards efficient energy storage.

state. Ethanol helps stabilize the 1T phase by interacting with the sulfur precursors and preventing its complete transformation into the more thermodynamically stable 2H phase. Therefore, the hydrothermal method, as well as the bottom-up approach enables better control over phase composition, morphology, and defect engineering, which collectively contribute to enhanced electrochemical behaviour (Fig. 1b).

Synthesis of 1T MoS_2@Cu_2S. For the preparation of the composite, 0.05 M of $CuCl_2 \cdot 2H_2O$ and 0.15 M of thiourea were solvated in EDA and stirred for 1 h to form a homogeneous

solution. To this solution, 225 mg of as-prepared 1T MoS_2 was added and again stirred for 1 h to make it completely dissolve in the solution. Afterwards, the solution was transferred to a 50 mL stainless steel autoclave and kept in a muffle furnace at 80 °C for 8 h at a heating rate of 1 °C min^{-1}. The black product was collected after centrifugation with DI water and with ethanol. The final product was kept in a hot air oven at 60 °C for 24 h. This was termed hy-1T MoS_2@Cu_2S (Fig. 1c).

The significant differences in the Cu_2S morphologies at different reaction temperatures are attributed to the effective coordination degree of EDA, which is a classic bidentate ligand used for its strong coordination ability with Cu^{2+} ions.[37] Temperature-dependent experiments in the presence of EDA were designed to understand the crystal growth behaviour of Cu_2S and its integration with MoS_2. At 60 °C, the nanostructures appeared as individual dendrites or small dendritic clusters (~1.2–1.5 μm in length, Fig. S1a in the ESI†). Upon increasing the synthesis temperature to 80 °C, snowflake-like architectures were formed, characterized by sixfold symmetrical dendritic petals measuring 4–5 μm in length (Fig. S1b in the ESI†). These structures showed further branching, with intersection angles of ~60°, indicating controlled anisotropic growth.[38] At 100 °C, however, the dendritic morphology was disrupted (Fig. S1c in the ESI†), and the structures transformed into sheet-like forms, suggesting the decomposition of EDA complexes due to its volatile nature at elevated temperatures. The clear progression in morphology with increasing temperature has been revealed by SEM analyses.

EDA forms a $[Cu(En)_2]^{2+}$ complex (where En stands for H_2N–CH_2–CH_2–NH_2) with the copper cation in the temperature range of 60–80 °C, which may first be the nucleation and crystal growth of Cu_2S and then formation of snowflake structures. However, at higher reaction temperatures (100 °C), the solution will result in the formation of a reduced complex due to the volatile nature of EDA. The formation of hy-1T MoS_2@Cu_2S involves the chelation of Cu^{2+} with EDA, followed by the reaction with thiourea as the sulfur source. The key chemical reactions can be represented as follows (eqn (1)–(4)):

Step 1: Chelation of Cu^{2+} with EDA

$$CuCl_2 \cdot 2H_2O + 2En \rightarrow [Cu(En)_2]^{2+} + 2Cl^- + 2H_2O \quad (1)$$

This chelated complex stabilizes Cu^{2+} in solution and controls its release for Cu_2S formation.

Step 2: sulfur release from thiourea

$$H_2N - CS - NH \rightarrow H_2S + \text{byproduct} \quad (2)$$

Thiourea decomposes at elevated temperatures, releasing H_2S, which acts as the sulfur source for Cu_2S formation.

Step 3: formation of the Cu_2S nanostructure

$$[Cu(En)_2]^{2+} + H_2S \rightarrow Cu_2S + 4En + 2H^+ \quad (3)$$

The released H_2S reacts with the Cu^{2+}complex to form Cu_2S nuclei, followed by crystal growth into a snowflake morphology.

Step 4: composite formation with 1T MoS_2

$$Cu_2S + 1T - MoS_2 \rightarrow 1TMoS_2@Cu_2S \quad (4)$$

The as-prepared 1T MoS_2 interacts with the Cu_2S, forming the hy-1T MoS_2@Cu_2S composite through electrostatic interactions and interfacial bonding.

Results and discussion

Morphological analysis

The morphological evolution of MoS_2 across different phases and synthesis methods, highlighting the impact of processing conditions on structural characteristics, is intensively illustrated in Fig. 2. Bulk-2H MoS_2 (Fig. 2a) shows a laminated structure, which breaks into irregular few-layered flakes after chitosan-assisted exfoliation (ex-2H MoS_2, Fig. 2b), potentially hindering the charge transport mechanism. In contrast, hydrothermally synthesized hy-2H MoS_2 (Fig. 2c) exhibits an unopened flake-like structure with a disc-shaped morphology due to slow nucleation and stacked flake formation in non-acidic media. In contrast, hy-1T MoS_2 displays well-defined, dispersed flakes (Fig. 2d). This transformation arises from the inclusion of ethanol and nitric acid, which influence nucleation kinetics by modifying the solvent properties, altering surface energy, and promoting controlled crystal growth.[39] As a result, 1T-phase MoS_2 achieves a more open, well-defined morphology, improving its electrochemical performance. Hence, the loss of structural integrity caused in ex-2H MoS_2 prepared through the top down approach can limit charge transport efficiency in energy storage applications compared to that of the bottom up approach. The introduction of Cu_2S into the hy-1T MoS_2 matrix further refines the morphology, leading to the formation of a distinct snowflake-like structure of the composite (Fig. 2e). Here, the presence of 1T-MoS_2 nanoflakes may provide a template, influencing the lateral growth of Cu_2S and enhancing anisotropic branching. The EDS analysis also supports the presence of Mo, S, and Cu in the composite (Fig. 2f). The high surface energy of 1T-MoS_2 allows Cu_2S to nucleate and grow along its layered structure, ensuring good composite formation. The synergistic interaction between MoS_2 and Cu_2S prevents excessive coalescence, further supporting the formation of well-defined branched dendritic structures. Hence, this snowflake-like morphology forms to minimize surface energy, leading to hierarchical structures that enhance electrolyte access and charge transfer. TEM analysis provides insight into the structural and crystallographic characteristics of the hy-2H MoS_2, hy-1T MoS_2 (Fig. S2a and b in the ESI†) and hy-1T MoS_2@Cu_2S composite. As observed in the TEM images (Fig. 2g), the composite exhibits a distinct six-fold symmetric morphology resembling a snowflake structure. This high degree of symmetry and structural order is indicative of controlled growth, which plays a crucial role in enhancing electrochemical performance. The SAED pattern (Fig. 2h) further verifies the single-crystalline nature of the material, displaying well-defined diffraction spots. Notably, the presence of multiple secondary diffraction spots, such as the six dim spots surrounding the central bright region (marked by arrows), confirms the formation of a double-folded periodic structure, a characteristic

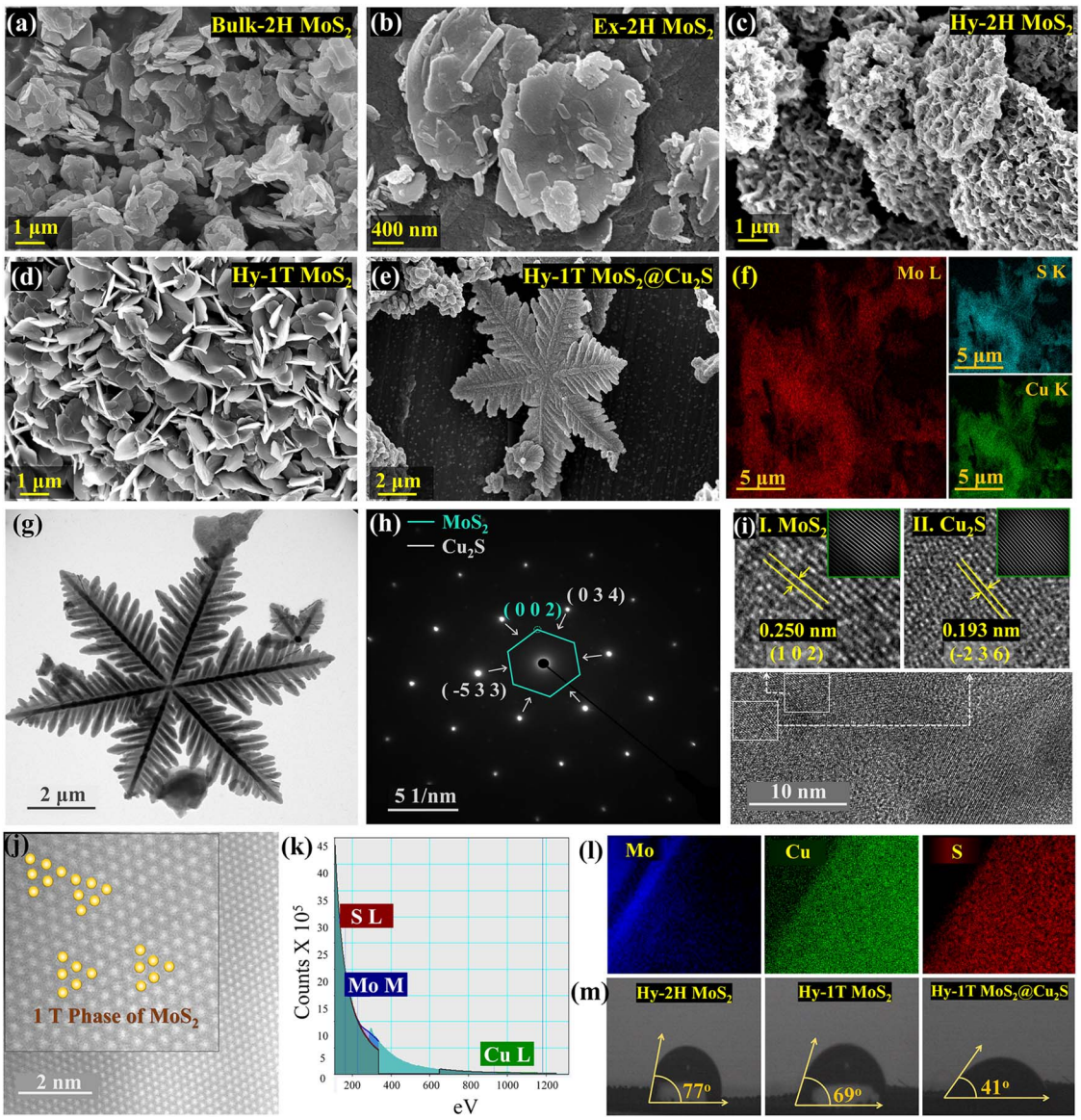

Fig. 2 FE-SEM images of (a) bulk-2H MoS_2, (b) ex-2H MoS_2, (c) hy-2H MoS_2, (d) hy-1T MoS_2, and (e) hy-1T MoS_2@Cu_2S at different magnifications, (f) elemental mapping (g) TEM images of hy-1T MoS_2@Cu_2S, (h) corresponding SAED pattern, (i) HRTEM images along with the FFT in the inset, (j) STEM image of hy-1T MoS_2@Cu_2S, (k) EELS spectrum, (l) elemental mapping of Mo, Cu and S, respectively and (m) static contact angle images of hy-2H MoS_2, hy-1T MoS_2 and hy-1T MoS_2@Cu_2S, respectively.

feature of the composite.[40] The SAED pattern distinctly identifies the coexistence of the 1T phase of MoS_2 along with Cu_2S. Specifically, the (002) plane of 1T-MoS_2 (highlighted with a green line) is followed by the (034) and (−533) planes of Cu_2S, further corroborating the successful integration of both phases. To gain deeper insight into the crystallographic properties of the composite, HRTEM imaging was performed (Fig. 2i, along with the FFT in the inset). This reveals two distinct sets of lattice fringes, confirming the structural coherence and successful formation of the heterostructure). In Fig. 2i.I, the measured d-spacing of 0.250 nm corresponds to the (102) plane of 1T-MoS_2, while in Fig. 2i.II, a d-spacing of 0.193 nm is attributed to the (−236) plane of Cu_2S. These interplanar spacings are in excellent agreement with XRD data, validating phase identification. Furthermore, HRSTEM imaging (Fig. 2j) highlights the trigonal symmetry of the 1T phase of MoS_2 (represented by yellow dots), confirming its abundant formation within the composite. The stabilization of the metallic 1T phase is crucial for achieving high electrical conductivity and improved charge transfer kinetics. Complementary elemental analysis *via* electron energy loss spectroscopy (EELS) provides further confirmation of the atomic composition, with distinct signals corresponding to S, Mo, and Cu (Fig. 2k). From the spectrum it can be revealed that the Mo-M edge shows a slight shift to lower energy, while the Cu–L edge exhibits a marginal shift to higher energy. This implies increased electron density around Mo atoms suggesting electron transfer from Cu_2S to MoS_2, which helps stabilize the metallic 1T phase and prevents its relaxation into the more

thermodynamically favoured 2H structure. Additionally, the fine structure observed in the S–L edge suggests the formation of new interfacial bonding environments, likely Mo–S–Cu bridges, that further contribute to electronic and structural stabilization of the 1T configuration. Elemental mapping (Fig. 2l) illustrates the homogeneous spatial distribution of these elements, indicating uniform integration of Cu_2S into the MoS_2 matrix. This uniformity is essential for ensuring consistent electrochemical activity across the electrode material, contributing to enhanced supercapacitor performance.

To further validate the increased surface energy of the composite compared to hy-2H MoS_2, contact angle measurements were performed (Fig. 2m). The contact angles for hy-2H MoS_2, hy-1T MoS_2, and hy-1T MoS_2@Cu_2S with 2 M KOH electrolyte were recorded to be 77°, 69°, and 41°, respectively. The significantly lower contact angle of the composite confirms enhanced hydrophilicity which ensures superior electrolyte wettability and improved electrochemical interaction, further reinforcing its suitability for energy storage applications.

Structural analysis

The crystal structure and phase composition of all MoS_2 samples and the composite material were identified using XRD spectra. As shown in Fig. 3a, the diffraction pattern of bulk 2H-MoS_2, which is commercially sourced and a highly ordered material, displays sharp and well-defined peaks due to its multilayer stacking and long-range order and aligns precisely with the standard reference JCPDS card no. 037-1492, confirming its phase purity. In the case of ex-2H MoS_2, the appearance of a diffraction peak at $2\theta \approx 21.3°$ is attributed to chitosan, indicating its successful intercalation between the MoS_2 layers. Notably, the diffraction intensity of chitosan is significantly diminished due to the dominant peaks of MoS_2. This intercalation process facilitated the exfoliation of bulk-2H MoS_2 while preserving the characteristic (002) lattice plane at $2\theta \approx 14.4°$, which confirms the retention of the 2H phase. However, the other peaks at $2\theta \approx 35°$, 39°, 50° and 59° appear in reduced intensity due to the reduction in the layer number, interlayer expansion, and introduction of functional groups and defects from the exfoliation process. These peak positions are in good agreement with that of bulk 2H MoS_2. But their XRD patterns indeed exhibit noticeable differences. These differences do not stem from a change in crystallographic phase but rather from layer stacking and structural integrity. For hydrothermally synthesized MoS_2 (hy-2H MoS_2), the XRD spectrum presents a rather diffused and low-intensity profile, which may be attributed to its formation *via* the hydrothermal reaction under moderate conditions that likely resulted in low stacking order, nanoscale domains, and possible structural disorder. For hy-2H MoS_2, three distinct diffraction peaks appear at $2\theta \approx 14.4°$, 33.6° and 59°, corresponding to the (002), (100), and (110) planes, respectively. The strong (002) peak at ~14.4° further confirms the formation of the 2H phase. In contrast, for hy-1T MoS_2, a notable shift in the (002) peak to a lower diffraction angle at ~9.5° is observed and the peak at ~14.4° vanishes, signifying the structural transition to the metastable 1T phase.[41] However, the (100) and (110) reflections remain unchanged, verifying the structural integrity of MoS_2. Upon the formation of the hy-1T MoS_2@Cu_2S composite, the persistence of the (002) peak at ~9.2° but a slight red shift in the angle indicates that the 1T phase is retained during composite synthesis and more defects are created due to incorporation of Cu_2S in the composite matrix.[42] Additionally, the appearance of new

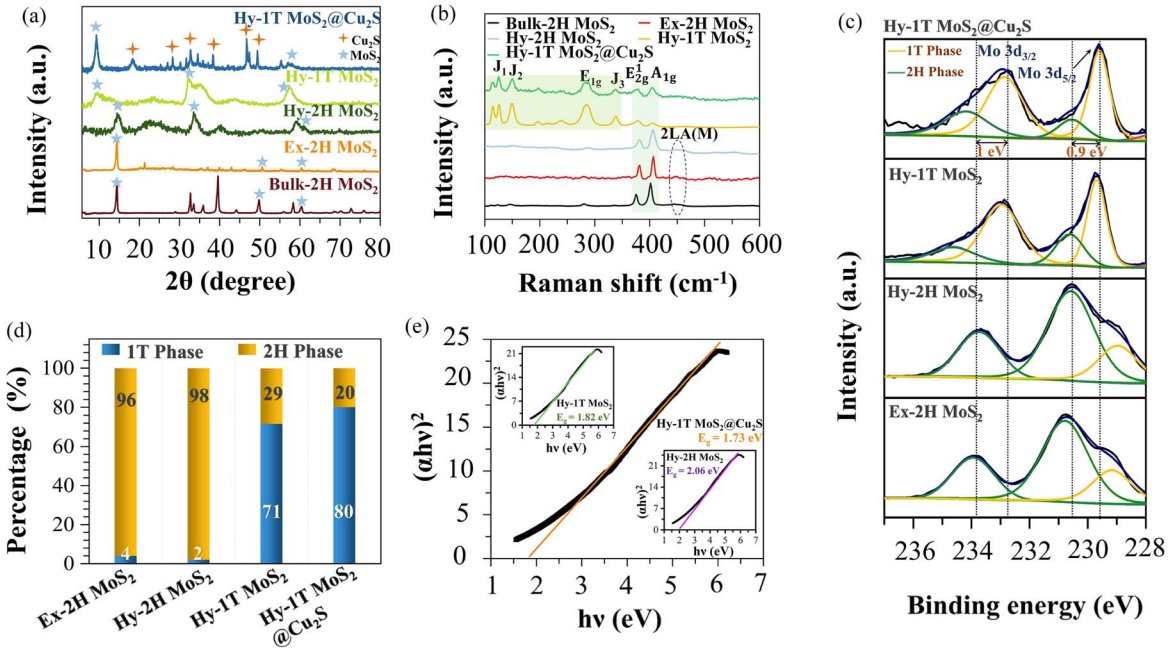

Fig. 3 Structural analysis of all the prepared MoS_2 and hy-1T MoS_2@Cu_2S composite. (a) XRD spectra, (b) Raman spectra,(c) XPS spectra of Mo 3d, (d) phase percentage of MoS_2 from deconvolution of XPS spectra, and (e) Tauc plot.

diffraction peaks characteristic of Cu_2S further substantiates the successful incorporation of Cu_2S. These peaks align well with the standard monoclinic Cu_2S phase (JCPDS card no. 007-1284; space group $P2_1/c$, 14), affirming the formation of the composite with well-defined crystallographic features. The standard references for MoS_2 and Cu_2S along with the XRD pattern of chitosan are provided in Fig. S3a and b in the ESI.† The average interlayer spacing (d) was calculated using Bragg's law (eqn S1 in the ESI†) for all MoS_2 samples and their composites to evaluate structural modifications upon exfoliation, phase transition, and composite formation. For ex-2H MoS_2, the interlayer spacing was determined to be 6.03 Å. In the case of hydrothermally synthesized hy-2H MoS_2, a slight increase to 6.16 Å was observed, which remains consistent with the reported literature value for the 2H phase.[43] A more substantial expansion in interlayer spacing was recorded for hy-1T MoS_2, where d increased to approximately 8.54 Å, confirming the successful formation of the metastable 1T phase. This value aligns well with previously reported data for 1T-MoS_2,[43] where the phase transition led to an increase in interlayer separation. Interestingly, upon the formation of the hy-1T MoS_2@Cu_2S composite, the interlayer spacing exhibited a significant increase to 11.13 Å, an expansion of nearly 3 Å compared to hy-1T MoS_2. This notable increase not only validates the successful incorporation of Cu_2S into the composite but also suggests a pronounced structural rearrangement by stabilizing the 1T phase of MoS_2. This expansion suggests interfacial interaction or partial intercalation of Cu_2S, which introduces strain and inhibits the close packing necessary for the 1T-to-2H transformation. The enlarged interlayer distance weakens interlayer van der Waals forces and physically constrains the lattice from reorganizing into the compact 2H phase. Moreover, the structural distortion introduced by interfacial bonding likely acts as a mechanical barrier, effectively pinning the lattice in the metastable 1T configuration. In addition, the microstructural parameters calculated from Scherrer's formula (eqn S2–S4 in the ESI†) support this conclusion. The composite exhibits a larger crystallite size, D (21.18 nm), and marked reductions in both dislocation density, δ (32.89 lines per nm), and microstrain, ε (16.27), compared to pristine 1T-MoS_2 (D = 3.18 nm, δ = 159.72 lines per nm, ε = 83.27) (all the values are provided in Table S1 in the ESI.† A phase transition from 1T to 2H typically leads to increased strain, higher defect density, and structural distortion, all of which are not observed in our composite. Instead, the data suggest lattice relaxation and improved structural order upon Cu_2S incorporation. Raman spectroscopy serves as a reliable characterization technique for confirming the phase identity of MoS_2. As shown in Fig. 3b, the characteristic vibrational modes of MoS_2 appear at 376 cm^{-1} and 402 cm^{-1}, corresponding to the in-plane Mo–S phonon mode (E_{2g}^1) and out-of-plane Mo–S phonon mode (A_{1g}), respectively. The in-plane (E_{2g}^1) mode is an outcome of the two S atoms and the Mo atom opposing each other, while A_{1g} mode is allied to the vibration of the two S atoms in opposite directions with a stationary Mo atom in between.[44] Another less intense peak at around 450 cm^{-1} arises from a second-order process involving the longitudinal acoustic phonons at M point 2LA(M).[45] These three peaks are very specific for the 2H phase. These peaks are distinctly observed in bulk-2H MoS_2 and remain visible in exfoliated MoS_2 (ex-2H MoS_2), verifying the successful exfoliation process and the formation of few-layer MoS_2. For hydrothermally synthesized hy-2H MoS_2, these three peaks are prominently present, confirming the retention of the 2H phase. However, in the case of hy-1T MoS_2, these three peaks are of less intensity and additional Raman peaks emerge in the lower frequency region at 145, 234, 280, and 334 cm^{-1}, which are assigned to the J_1, J_2, E_{1g}, and J_3 photon modes, respectively.[46] These low-frequency modes are distinctive signatures of the 1T phase, arising from its octahedral coordination and enhanced electron–phonon coupling effects.[47] Importantly, these characteristic 1T-MoS_2 peaks persist in the Raman spectrum of the hy-1T MoS_2@Cu_2S composite, confirming that the 1T phase is retained even after composite formation. The structural integrity of 1T-MoS_2 within the composite suggests that Cu_2S incorporation does not disrupt the metastable phase but rather stabilizes it, which could be advantageous for electrochemical applications where enhanced conductivity and charge storage capabilities are desired. The results of FT-IR and BET are discussed in Fig. S4 and Table S2 in the ESI.†

The experiment of XPS was carried out not only to solely determine the oxidation state of the elements, but also to ensure the distinct phases of MoS_2, in the synthesized samples. These binding energies are highly sensitive to the local chemical and electronic environments of the atom, including factors such as coordination geometry, electron density, and screening effects. As shown in Fig. 3c, the high-resolution Mo 3d spectrum provides insight into the oxidation state of Mo and phase distribution of MoS_2. The peaks near ~233 eV and 230 eV are indexed to Mo $3d_{3/2}$ and Mo $3d_{5/2}$, respectively. The Mo 3d doublet, consisting of Mo $3d_{3/2}$ (~230 eV) and Mo $3d_{5/2}$ (~233 eV), was deconvoluted into four distinct peaks to differentiate between the 2H phase and the 1T phase.[41] These two phases exhibit markedly different structural and electronic characteristics. The 2H phase possesses a trigonal prismatic coordination geometry and is semiconducting in nature, resulting in relatively localized electrons and reduced electronic screening around the Mo centre. This leads to higher observed binding energies in the Mo 3d region *i.e.* at ~230 eV and ~234 eV. Conversely, the 1T phase adopts an octahedral coordination geometry and displays metallic behaviour, which facilitates increased delocalization of electrons and enhanced electronic screening. This greater screening effectively reduces the energy required to eject core-level electrons, thereby resulting in a downward shift of ~0.9 V in the Mo 3d binding energies at ~229 eV and ~233 eV in the XPS spectrum.

Therefore, it can be clearly seen that for ex-2H MoS_2 and hy-2H MoS_2, the deconvoluted peaks corresponding to Mo $3d_{3/2}$ and Mo $3d_{5/2}$ states of Mo^{4+} at ~230.7 and 233.9 eV are present predominantly, establishing their 2H phase over the 1T phase. Notably, hy-2H MoS_2 shows an even lower (2%) 1T phase content compared to ex-2H MoS_2 (4%), reinforcing that the bottom-up hydrothermal synthesis preferentially stabilizes the 2H phase (Fig. 3d). In contrast, for hy-1T MoS_2 and hy-1T MoS_2@Cu_2S, four deconvoluted peaks are assigned to ~233,

234, 229.7, and 230.6 eV. The former two peaks are attributed to Mo $3d_{3/2}$ of 1T and 2H phases, whereas the latter two peaks are generated due to the Mo $3d_{5/2}$ state of 1T and 2H phases, respectively. It can be seen that the energy difference between the peaks of 1T and 2H phases is almost 0.9–1 eV for both the cases. Quantitative analysis further reveals that the 1T concentration percentage is significantly higher than that of 2H. Specifically, hy-1T MoS_2 reaches 71%, whereas hy-1T MoS_2@Cu_2S reaches an impressive 80% (Fig. 3d), highlighting that the integration of Cu_2S promotes and stabilizes the metallic 1T phase. This stabilization can be attributed to interfacial interactions between MoS_2 and Cu_2S, which reduce structural distortions and enhance electron delocalization, thereby favouring the retention of the metastable 1T phase. The survey scan of the composite, S 2p spectra and Cu 2p spectra are discussed in the ESI (Fig. S5 and Table S3).† Additionally, ICP-AES measurements have been conducted by taking 4 ppm solution of hy-1TMoS_2@Cu_2S; the atomic ratios are found to be 20.5% of Mo, 26.6% of Cu and 52.9% of S.

For optical analysis, UV-visible spectroscopy was performed to ensure the band gap energy of the synthesised MoS_2. Hy-2H MoS_2, hy-1T MoS_2 and hy-1T MoS@Cu_2S have shown strong absorbance near 294 nm (Fig. S5d in the ESI†). The band gap energy of these three materials was estimated using the Tauc plot equation (eqn S5 in the ESI†) following the direct allowed transition (Fig. 3e). The calculated bandgap energy for hy-2H MoS_2 is 2.06 eV, whereas for hy-1T MoS_2, it was found to be 1.88 eV. A slight decrease of 0.1 eV can be observed in the case of hy-1T MoS_2@Cu_2S.

Electrochemical activity of the prepared materials

A detailed investigation of the electrochemical performance of the synthesized materials was carried out through extensive electrochemical measurements using a three-electrode system. A comparative study was carried out on all the phases of MoS_2, along with the hy-1T MoS_2@Cu_2S composite, using 2 M KOH as the electrolyte as shown in Fig. 4a. The voltage range was consistently maintained between −0.8 V and 0.2 V for all components across a wide range of scan rates, varying from 1 to 2000 mV s^{-1}, to ensure a uniform evaluation of their electrochemical behaviour. Notably, the CV analysis revealed distinct electrochemical characteristics for the composite material compared to the individual phases of MoS_2. The 2H and 1T phases of MoS_2 exhibited EDLC behaviour, as evidenced by their nearly rectangular CV profiles with minimal redox peaks (Fig. S6(a–d) in the ESI†). This indicates that these phases primarily rely on charge storage through ion adsorption at the electrode–electrolyte interface, characteristic of EDLC-type capacitive behaviour.[48] In contrast, the hy-1T MoS_2@Cu_2S composite demonstrated a significantly different CV curve, exhibiting well-defined anodic and cathodic peaks, which suggests a pronounced faradaic redox mechanism. The presence of these peaks confirms the pseudocapacitive nature of the composite, where charge storage is not limited to electrostatic adsorption but also involves redox reactions. This electrochemical behaviour can be attributed to a greater number of metal active centres and synergistic interactions between MoS_2 and the Cu_2S matrix, which facilitate fast charge transfer. Also, the results clearly indicated that the hy-1T MoS_2@Cu_2S

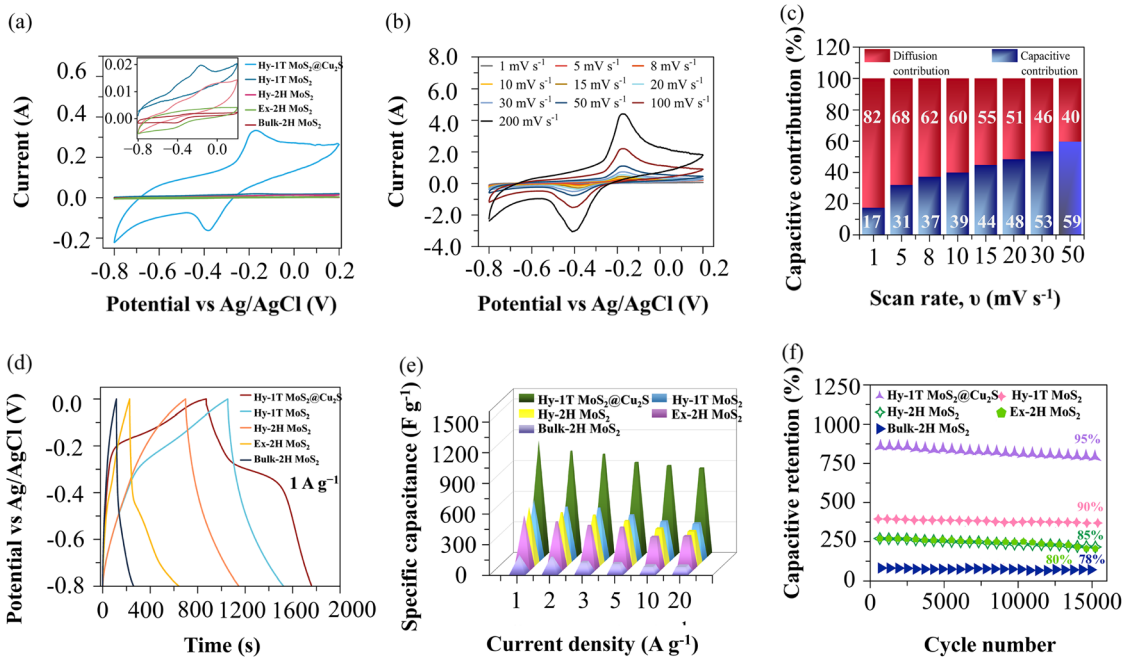

Fig. 4 (a) Comparison of electrochemical activity among bulk-2H MoS_2, ex-2H MoS_2, hy-2H MoS_2, hy-1T MoS_2 and hy-1T MoS_2@Cu_2S, (b) CV graph of hy-1T MoS_2@Cu_2S at difference scan rates, (c) contribution ratio of diffusion and capacitive contributions with respect to the scan rate, comparative analysis among bulk-2H MoS_2, ex-2H MoS_2, hy-2H MoS_2, hy-1TMoS_2 and hy-1T MoS_2@Cu_2S, (d) GCD curves at 1 A g^{-1}, (e) C_{sp} at different current densities, and (f) capacitance retention at 20 A g^{-1}.

composite exhibited the highest current response and enclosed the largest area under the CV curve, thereby demonstrating superior electrochemical performance compared to the individual MoS_2 phases. The improved performance can be attributed to multiple factors, such as the increased conductivity provided by the 1T phase of MoS_2, the enhanced electroactive sites contributed by the Cu_2S component, and the overall structural stability and efficient electron/ion transport within the composite material. Furthermore, among the individual MoS_2 phases, hy-1T MoS_2 showed better electrochemical performance than as-synthesized 2H MoS_2. This superiority arises from the intrinsic metallic nature of the 1T phase, which significantly enhances electrical conductivity and facilitates rapid charge transport. Additionally, the hy-2H MoS_2 phase exhibited improved performance compared to ex-2H MoS_2, suggesting that the structural modifications achieved *via* the specific synthesis route play a crucial role in enhancing electrochemical activity.

Further investigations on CV were conducted using the hy-1T MoS_2@Cu_2S composite as a working electrode. The voltammograms exhibit a uniform profile across all scan rates (1–50 mV s^{-1}), demonstrating consistent charge transfer dynamics as shown in Fig. 4b. The oxidation and reduction peaks arise from electrochemical interactions between the electrolyte species and the active metal centres within the composite. These faradaic processes are influenced by the applied scan rate, which directly modulates the current response. An increase in the scan rate enhances the current due to the accelerated potential sweep, following the Randles–Sevcik equation presented below:

$$i_p = 2.69 \times 10^5 n^{3/2} A C D^{1/2} \nu^{1/2} \quad (5)$$

where i_p is the peak current in A, n is the number of electrons that participated in the redox reaction, A is the area of the working electrode in cm^2, C is the concentration of redox species in mol cm^{-3}, D is the diffusion coefficient of the redox species in $cm^2\ s^{-1}$ and ν is the scan rate in mV s^{-1}. This nature of curve proves the electro-kinetic process to be diffusion-controlled (Fig. S7a in the ESI†).

As the scan rate increases, a noticeable shift in peak potential is observed. The anodic peak progressively moves towards a more positive potential, while the cathodic peak shifts towards a more negative potential. In an ideal electrochemically reversible process, the anodic-to-cathodic peak current ratio (ip_a/ip_c) should be 1, and the peak-to-peak separation (ΔE_p) is expected to be 57 mV at 25 °C. This small ΔE_p value signifies rapid and efficient electron transfer kinetics, where the energy barrier for redox reactions is minimal, allowing the system to maintain Nernstian equilibrium almost instantly in response to applied potential changes.

However, in this study, the observed average ip_a/ip_c ratio is > 1(~1.74), and the average ΔE_p across all scan rates is significantly higher at 230 mV. Such deviations indicate that the system exhibits quasi-reversible behaviour. The large ΔE_p suggests a substantial energy barrier for the transition between oxidized and reduced species, leading to sluggish heterogeneous electron transfer kinetics at the electrode–electrolyte interface. As a result, an additional potential, known as overpotential, is required to drive the redox reactions to completion.

Furthermore, at higher scan rates, the interaction time between electrons and the electrode surface is reduced, further hindering the redox reaction. To counteract these limitations, an increase in the scan rate shifts the potential to higher values, facilitating the redox process through polarization and overpotential effects.

The equations involving the redox reactions (eqn (6)–(8)) are as follows:[49]

$$MoS_{2(surface)} + K^+ + e^+ \rightarrow (MoS_2 - K^+)_{surface}(\text{Non-Faradaic}) \quad (6)$$

$$MoS_2 + K^+ + e^+ \rightarrow MoS_2 - SK(\text{Faradaic}) \quad (7)$$

$$Cu_2S + OH^- \rightarrow Cu_2SOH^- + e^- \quad (8)$$

The charge storage mechanism primarily consists of two approaches: the surface-controlled capacitive process and the diffusion-controlled faradaic process. The capacitive process is driven by reversible ion adsorption at the electrode–electrolyte interface, resulting in EDLC. In contrast, the diffusion-controlled process occurs within the bulk material, exhibiting battery-like behaviour. To analyse the charge transfer dynamics, the power law is employed (eqn (9)):

$$i = a\nu^b \quad (9)$$

where i is the peak current, ν (mV s^{-1}) is the corresponding scan rate, and a and b represent constants that help describe the electrochemical process based on experimental data. This equation can be expressed as (eqn (10)):

$$\log(i) = \log(a) + b\log(\nu) \quad (10)$$

The parameter b can be determined from the slope of the linear relationship between $\log(i)$ and $\log(\nu)$ (Fig. S7b in the ESI†). A b value of 0.5 indicates a diffusion-controlled capacitive process, whereas a value close to 1 signifies a surface-controlled dominant contribution. For hy-1TMoS_2@Cu_2S, the calculated b value is 0.5, classifying it as a pseudocapacitive material. The overall capacitance enhancement is attributed to both diffusion-controlled and surface-controlled mechanisms. The relative contributions of these processes at a given potential can be quantified using Dunn's method (eqn (11)), where $k_1\nu$ represents the surface-controlled component and $k_2\nu^{1/2}$ corresponds to the diffusion-controlled component. Here, k_1 and k_2 are scan rate-independent constants.[50]

$$i = k_1\nu + k_2\nu^{1/2} \quad (11)$$

For analytical purposes this can be written as:

$$i/\nu^{1/2} = k_1\nu^{1/2} + k_2 \quad (12)$$

Both the parameters k_1 and k_2 can be evaluated from the slope and intercept value, respectively, of the linear plot of $i/\nu^{1/2}$ *vs.* $\nu^{1/2}$ presented in Fig. S7c in the ESI.† The best linear fitting of the plot ($R^2 = 0.92$) gives the values of k_1 and k_2 as 0.013 and

0.062, respectively, for hy-1TMoS$_2$@Cu$_2$S. Using these values of k_1 and k_2, the contribution ratio of the capacitive controlled process and diffusion controlled process can be calculated. As shown in Fig. 4c, the diffusion controlled surface redox reaction reaches ~84% at lower scan rates and gradually decreases to ~40% while increasing the scan rate, as electrolyte ions gets less time to react with electroactive materials and hence a sluggish charge transfer reaction takes place.

To gain deeper insight into the electrochemical behaviour of the synthesized materials, we performed GCD measurements of all the synthesized MoS_2 and the composite by applying a current against a voltage window of −0.8–0 V *vs.* Ag/AgCl. The nature of the GCD curves closely aligns with the CV profiles, confirming consistency in the charge storage mechanism. The comparative GCD curve at 1 A g^{-1} of the as-prepared MoS_2 shows linear and symmetric triangular GCD profiles indicative of a typical EDLC type material, primarily governed by surface-controlled charge storage, whereas hy-1TMoS$_2$@Cu$_2$S exhibits a pseudocapacitive, specifically, battery type nature evident from the characteristic humps in its charge–discharge profiles. These humps indicate the presence of faradaic redox reactions, which contribute to enhanced energy storage. Fig. 4d shows that the composite shows the highest discharge time among the others, demonstrating its superior charge storage capability. The GCD curves at current densities of 1, 2, 3, 5, 10, 15 and 20 A g^{-1} are shown in Fig. S8(a–d) in the ESI† for all the prepared MoS_2 materials. Across all these current densities, unlike EDLC, the hy-1TMoS$_2$@Cu$_2$S composite displays highly symmetrical non-linear charge–discharge curves with evident voltage plateaus (Fig. S8e in the ESI†). These plateaus are strong indicators of diffusion-controlled redox reactions, where charge is stored *via* electron transfer involving changes in the oxidation states of the active material. This nature of the curve typically implies a battery-type behaviour that originates from the intrinsic properties of the composite components. Here, 1T-MoS_2 has a metallic nature with a distorted octahedral coordination and high electrical conductivity, which facilitates rapid electron transport. More importantly, its expanded interlayer spacing allows intercalation of electrolyte ions (*i.e.* K^+) into the layers, similar to insertion-type battery electrodes. The other component, Cu_2S, a typical conversion-type transition metal sulphide, undergoes reversible redox reactions (*e.g.*, Cu^{2+}/Cu^+) during cycling. These reactions involve a change in the chemical state and structure of the material, contributing to higher specific capacities, longer charge–discharge times and excellent electrochemical stability. Furthermore, the small iR drop observed in the GCD curves is indicative of the composite's superior electrical and ionic conductivity.[51,52] This suggests minimal internal resistance, which is further corroborated by the low values of solution resistance (R_s) and charge transfer resistance (R_{ct}) obtained from electrochemical impedance spectroscopy (EIS) measurements.[53] The specific capacitance and areal capacitance of all the MoS_2 materials and the composite were calculated using the eqn (S6) in the ESI.† At a current density of 1 A g^{-1}, hy-1TMoS$_2$@Cu$_2$S exhibits a remarkable C_{sp} of 1118 F g^{-1} (C_s of 895 C g^{-1}). This high capacitance value highlights the superior charge storage capability of the composite material compared to pristine MoS_2. The C_{sp} value of hy-1TMoS$_2$@Cu$_2$S gradually decreases on increasing the current density from 1 A g^{-1} to 20 A g^{-1}. The value of C_{sp} for 1T MoS_2 at 1 A g^{-1} (585 F g^{-1}) is almost 50% lower than that of the composite, reinforcing the beneficial impact of Cu_2S incorporation in enhancing charge storage properties. Among the synthesized MoS_2 materials, the 1T phase consistently outperforms the 2H phase. This is because the 1T phase has a more metallic nature, improved electrical conductivity, and a higher density of active sites, which facilitate more efficient charge transfer and ion diffusion. In Fig. 4e, the trend of C_{sp} at all current densities is depicted clearly with a bar chart for as-synthesised MoS_2 and the composite (given in Table S4a in the ESI†). The areal capacitance of as-synthesised MoS_2 and the composite are also given in Table S4b in the ESI.†

To acquire a better understanding of the fundamental charge storage mechanism and the resistive characteristics of the system, EIS measurements were conducted in the frequency range of 0–100 kHz. The Nyquist plot (Fig. S8f in the ESI†) clearly demonstrates that bulk 2H-MoS_2 exhibits a much higher R_{ct} of 49.14 Ω, indicating that the multilayer structure of MoS_2 acts as a barrier to ion diffusion. This increased resistance hinders electrolyte penetration and slows down the redox reactions, leading to inefficient charge storage. The high R_{ct} value for bulk 2H-MoS_2 suggests that the presence of multiple stacked layers impedes ion accessibility, reinforcing the advantage of structural modifications or compositing strategies in enhancing electrochemical performance. Among the individual MoS_2 phases, few layered 1T MoS_2 exhibits a lower bulk resistance ($R_s = 1.24$ Ω) compared to hy-2H MoS_2 ($R_s = 2.16$) and ex-2H MoS_2 ($R_s = 2.18$), which can be directly linked to its metallic nature and intrinsic high electrical conductivity. The lower bandgap energy of 1T MoS_2 facilitates efficient charge transfer kinetics, significantly reducing interfacial resistance. Moreover, the rapid electron transport characteristic of 1T MoS_2 minimizes energy loss, leading to a lower R_s. While 1T MoS_2 is often considered thermodynamically less stable, its stability and electrochemical performance can be greatly enhanced through doping or compositional modifications. Hence, by incorporating Cu_2S into its distorted octahedral structure, the overall structural integrity and conductivity are improved, ensuring its long-term stability as a high-performance supercapacitor material. Therefore, inevitably, hy-1TMoS$_2$@Cu$_2$S has a significantly low R_s of only 1.16 Ω and R_{ct} of 8.29 Ω. Additionally, the linear portion of the Nyquist plot corresponds to Warburg impedance (W_0), which arises due to the diffusion-limited movement of reactant ions through the electrolyte. A steeper slope of 78° with respect to the *x*-axis (which is close to an ideal value of 90°) of hy-1TMoS$_2$@Cu$_2$S in this region is indicative of enhanced capacitive behaviour and efficient ion diffusion within the system, confirming its superior capacitive characteristics. Hence, this remarkable reduction in resistance is attributed to the synergistic interaction between 1T MoS_2 and Cu_2S which enhances both electronic conductivity and ion transport at the electrode–electrolyte interface. The R_s and R_{ct} values of all the synthesised elements are tabulated in Table S5 in the ESI.† Cycle stability is an important parameter to evaluate

the stability and integrity of the electrode material. The incorporation of Cu_2S in the 2D structure of 1T MoS_2 helps in formation of a stable composite as an effect of synergism. The snowflake-like morphology provides a mechanical reinforcement in order to maintain its structural integrity. The well-defined conductive network of Cu_2S ensures that the MoS_2 layers remain well-dispersed, preventing material aggregation that could degrade performance over extended cycling. During repeated ion intercalation and deintercalation, electrode materials experience mechanical stress. The composite effectively absorbs these structural changes, reducing internal strain and preventing material degradation. As a result, the composite retains 95% of its capacitance even after 15 000 charge–discharge cycles at a high current density of 20 A g^{-1}, highlighting its exceptional electrochemical durability and structural robustness as compared to the other different phases of MoS_2 (Fig. 4f).

A comparative analysis is presented in Table S6 in the ESI,† highlighting the superior electrochemical performance in terms of morphology, specific capacitance, and key features of the reported literature values. Additionally, a composite using hy-2H MoS_2 was also synthesised. The detailed comparative discussion between hy-2H MoS_2@Cu_2S and hy-1T MoS_2@Cu_2S is appended in the ESI (Fig. S9).†

Asymmetric hybrid supercapacitor (AHSC) device performance

Following a thorough assessment of the electrochemical performance of different MoS_2 phases and their composites, an asymmetric hybrid supercapacitor (AHSC) device was assembled using hy-1TMoS_2@Cu_2S as the anode and MnO_2 as the cathode. MnO_2 was synthesized following our previously reported work[50] and all the necessary characterization studies followed by electrochemical properties are detailed in Fig. S10 and S11 (ESI).† Both the electrode materials were uniformly coated onto SS current collectors, ensuring good adhesion and conductivity. PVA-KOH gel was employed as the separator to facilitate ionic transport. The use of PVA-KOH gel electrolyte ensures strong ion transport efficiency while mitigating unwanted side reactions that typically degrade supercapacitor performance at higher voltages. To achieve an optimal potential window with enhanced energy and power density, precise control over mass loading was maintained using the charge balance equation (eqn S7 in the ESI†), with the mass ratio (m^+ :

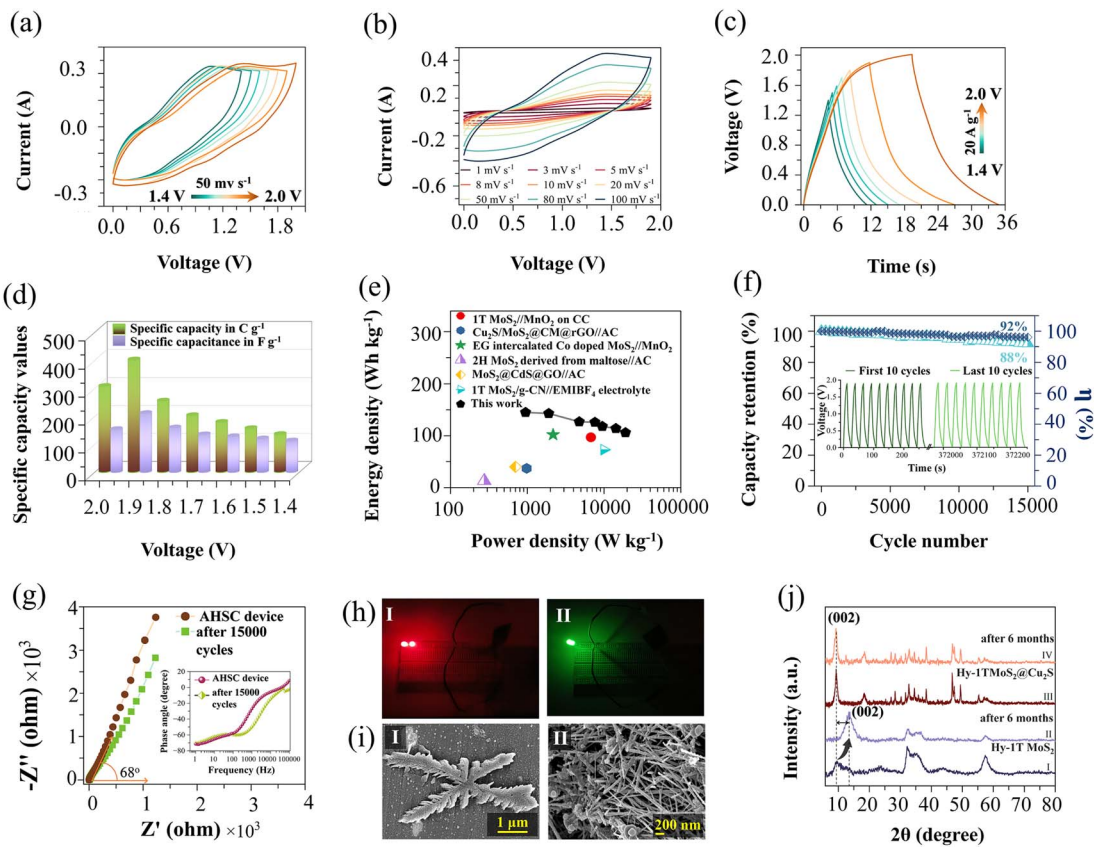

Fig. 5 Electrochemical study of the assembled hy-1TMoS_2@Cu_2S//MnO_2 asymmetric hybrid device: (a) CV curves of the device in various potential windows, (b) CV curves at varying scan rates, (c) GCD curves of the device in varying voltage windows, (d) C_s and C_{sp} values in C g^{-1} and F g^{-1}, respectively, (e) Ragone plot of the device compared with other reported work, (f) cycle stability test showing retention of capacitance at 10 A g^{-1} after 15 000 cycles, (g) Nyquist plot showing the response of the device initially and after the cycle stability test with the Bode plot of the same in the inset, (h) illumination of two red LEDs and one green LED using the AHSC device, (i) SEM images of hy-1TMoS_2@Cu_2S and MnO_2 after the cycle stability test, and (j) XRD spectra of hy-1TMoS_2 and hy-1TMoS_2@Cu_2S before and after six months.

m^{-}) set at 4.5 : 1. The fabricated hy-1TMoS$_2$@Cu$_2$S//PVA-KOH//MnO$_2$ AHSC device underwent extensive electrochemical testing to validate its suitability as a supercapacitor. The CV response recorded at 10 mV s^{-1} (Fig. S12a in the ESI†) illustrates the operational voltage range for both the anode and cathode materials, confirming their stable operation across a broad potential range. To determine the most efficient working potential, CV was conducted at a scan rate of 50 mV s^{-1} by gradually extending the potential range from 0–1.4 V to 0–2.0 V through successive increments allowing evaluation of electrochemical stability and capacitive performance at higher voltages (Fig. 5a). From this analysis, it was established that 0–1.9 V is the optimal voltage window, ensuring both maximum charge storage and electrochemical stability without excessive polarization or side reactions. CV scans conducted at 1 to 100 mV s^{-1} (Fig. 5b) exhibited a consistent curve shape across all scan rates, demonstrating good capacitive behaviour and excellent charge storage characteristics. The preservation of the CV profile at higher scan rates highlights the well-polarized nature of the device, confirming its stable electrochemical performance. To complement the CV results, GCD measurements were conducted across voltage ranges from 0–1.4 V to 2 V at a high current density of 20 A g^{-1} (Fig. 5c). The C_{sp} and C_s values were calculated (Fig. 5d) to assess the effect of voltage variations on energy storage capabilities. In an optimal voltage range of 0–1.9 V, the device exhibited a C_s of 551 C g^{-1} and a C_{sp} of 290 F g^{-1}, outperforming the 0–2 V range in terms of efficiency. Beyond 1.9 V, a decline in C_{sp} was observed, due to excessive overpotential leading to sluggish charge transfer, increased internal resistance, and inefficient electron/ion transport, negatively affecting capacitance retention. Therefore, 0–1.9 V was identified as the most suitable voltage window for performing the GCD analysis as well as for achieving high energy (E) and power density (P) while ensuring long-term stability. A wider voltage window not only enhances the energy storage capability but also enables higher operating voltages, reducing the need for multiple devices in series and simplifying circuit integration for practical applications. Keeping this in consideration, GCD measurements were conducted at different current densities ranging from 1 to 20 A g^{-1} (Fig. S12b in the ESI†). The corresponding GCD curves are consistent, ensuring the robustness of the device. The C_{sp} value of the device increases to 290 F g^{-1} at 1 A g^{-1} and is able to sustain up to 211 F g^{-1} upon increasing the current densities (Fig. S12c in the ESI†).

The AHSC device demonstrated a remarkable energy density of 144 Wh kg^{-1} at 1 A g^{-1}, while maintaining a high power density of 950 W kg^{-1}. Notably, even at a significantly higher current density of 20 A g^{-1}, the device preserved an impressive energy density of 106 Wh kg^{-1}, with the power density reaching 19 000 W kg^{-1}. This impressive retention highlights the device's capability to maintain efficient charge storage and fast discharge even under high power conditions. A detailed comparison through the Ragone plot (Fig. 5e) highlights the superior performance of this AHSC in contrast to numerous previously reported materials (listed in Table 1).

The AHSC device was tested for its long term cyclability where it outperformed until 15 000 cycles with 92% capacitance retention and 88% coulombic efficiency (Fig. 5f). Furthermore, from impedance study (Fig. 5g), it was found that the AHSC device results in an extremely low R_s value of 0.61 Ω, reflecting minimum resistance as well as a minimal R_{ct} value of 20.12 Ω, signifying smooth charge-transfer kinetics. The capacitive nature of the device is evident from the linear segment of the Nyquist plot. Ideally, a capacitor makes a line forming a 90° angle with the x-axis in the low-frequency region. In this case, the linear segment maintains a 68° angle with the x-axis indicating a predominantly capacitive behaviour with a trivial influence of diffusion-limited charge transport. Further insights into the device's frequency response are obtained from the Bode plot. A phase angle of −71.5° confirms the AHSC's functionality as a hybrid capacitor. The knee frequency (f_0) is at 365.2 Hz, thereby calculating the corresponding relaxation time (τ_0) using the formula, $\tau_0 = \frac{1}{2}\pi f_0$, to be 0.4 s. This significantly low relaxation time accentuates facile ion diffusion and transport within the AHSC, supporting its extraordinarily high power density of 19 kW kg^{-1}. The impedance study is also performed after the stability test of 15 000 cycles and the device retains its robust nature showing a R_s value of 1.45 Ω and R_{ct} value of 22.62 Ω (Fig. 5g). Also, a slight phase angle shift to −70.2° in the Bode plot was observed. To validate the practical applicability of the device, two AHSC units connected in series were successfully used to power two red LEDs and a green LED and they remained lit up for about two minutes. The faradaic redox reactions of the device provide a sustained and stable voltage output during discharge. This prevents sudden voltage drops and ensures that the LED receives power for a longer time without flickering or dimming (Fig. 5h.I and II). The ability to power electronic devices directly highlights the device's scalability and effectiveness in delivering instantaneous power when required. To

Table 1 A comparison table of the performance of the devices from the literature

Device	ΔV(V)	Retention cycle	Energy density (Wh kg^{-1})	Power density (W kg^{-1})	Ref.
1 T MoS$_2$//MnO$_2$ on carbon cloth	1.8	86.4% after 5000 cycles	97	6733	41
Cu$_2$S/MoS$_2$@CM@rGO//AC	1.5	86.9% after 5000 cycles	36.9	981.8	54
Ethylene glycol intercalated Co doped MoS$_2$//MnO$_2$	1.6	99.2% after 10 000 cycles	102.7	2166.9	42
2H MoS$_2$ derived from maltose//AC	1.1	86.7% after 10 000 cycles	12.7	275.25	55
MoS$_2$@CdS@GO//AC	1.4	86.9% after 5000 cycles	40.69	700	12
1T- MoS$_2$/g-CN//EMIBF$_4$//1T-MoS$_2$/g-CN	2.5	91% after 10 000 cycles	73	10 000	56
Hy-1T MoS$_2$@Cu2S	1.9	92% after 15 000 cycles	144	19 000	Our work

further confirm the morphological stability of the electrode materials, post-cycling SEM analysis was performed on the hy-1TMoS$_2$@Cu$_2$S composite (Fig. 5i.I) and MnO$_2$ cathode (Fig. 5i.II). The images reveal that the composite retains its fundamental structure despite prolonged electrochemical operation, emphasizing its mechanical resilience and suitability for long-term supercapacitor applications. Post-cycling TEM analysis was also performed at different magnifications to assess the morphological stability of the 1T-MoS$_2$@Cu$_2$S electrode. These TEM images offer insightful structural evidence; in one micrograph (Fig. S14a†), a broken dendrite is clearly visible, suggesting partial mechanical degradation during long-term charge–discharge cycling. In another image (Fig. S14b†), only a portion of a dendritic branch remained, indicating that while the overall dendritic framework persists, localized fragmentation may occur due to repeated ion insertion/extraction and associated structural stress. The stability of the 1T phase was assessed by conducting XRD analysis on hy-1T MoS$_2$ and hy-1T MoS$_2$@Cu$_2$S after six months, given the tendency of 1T MoS$_2$ to transition into the more stable 2H phase over time. Notably, in hy-1T MoS$_2$, the characteristic (002) peak shifted from 9° to 14.2°, indicating a phase transformation (Fig. 5j I and II). However, in the hy-1T MoS$_2$@Cu$_2$S composite, the (002) peak remained unchanged, confirming that the 1T phase was successfully stabilized (Fig. 5j.III and IV). This finding unambiguously suggests that Cu$_2$S plays a crucial role in providing electronic shielding and structural confinement, preventing the phase transition and ensuring the long-term stability of the 1T phase.

Conclusion

This study presents a systematic, phase-guided approach to designing high-performance MoS$_2$-based supercapacitor materials. By comparing the 2H and 1T phases synthesized through exfoliation and hydrothermal methods, we identified the 1T phase as electrochemically superior due to its metallic nature. Notably, the bottom-up hydrothermal synthesis proved highly effective in controlling crystallinity and stabilizing the metastable 1T phase, preserving its conductive properties essential for energy storage. To overcome the remaining challenges of limited active sites and structural instability, Cu$_2$S was incorporated into the 1T-MoS$_2$ matrix, forming a novel hierarchical hy-1TMoS$_2$@Cu$_2$S composite. The snowflake-like morphology of Cu$_2$S combined with the layered MoS$_2$ structure facilitates rapid ion/electron transport, buffers volume changes, and enhances mechanical and cycling stability. This synergistic architecture enabled a high specific capacitance of 1118 F g^{-1}, with an impressive energy density of 141 Wh kg^{-1} and power density of 19 kW kg^{-1} in device configuration. Overall, our findings highlight the critical role of phase engineering and composite integration in advancing next-generation supercapacitor technologies.

Data availability

Data will be available from the author upon reasonable request.

Author contributions

Arkapriya Das: conceptualization, methodology, data collection and analysis, manuscript writing, Alakananda Paul: assisted in experiments and data collection, Ankita Mondal: discussion and validation, Kaushik Pal: overall research guidance, discussion, manuscript reviewing, editing and validation, and Bhanu Bhusan Khatua: overall research guidance, discussion, manuscript reviewing, editing and validation.

Conflicts of interest

The authors declare no competing financial interest.

Acknowledgements

This work was supported by the Department of Science and Technology (DST), Govt. of India, by providing the INSPIRE fellowship. The authors also acknowledged the central research facility (CRF) the Indian Institute of Technology Kharagpur for providing characterization facilities. The authors are also thankful to Ms. Sayantika Kar for helping with data collection of UV-visible spectroscopy. The authors also acknowledged the Indian Institute of Technology Roorkee for providing the lab facility.

References

1 S. P. Sadavar, S. V. Mulik, P. A. Koyale, S. V. Sadavar and S. D. Delekar, *Mater. Horiz.*, 2025.
2 M. A. Yewale, S. V. Desarada, A. M. Teli, K. B. Chavan, P. J. Morankar, D. K. Shin and S. T. Choi, *Energy Fuels*, 2025, **39**, 2281–2293.
3 Y. Liu, Y. Zhang, C. Yang, M. W. Shahzad, Y. Yan, L. Dai, W. Lu, W. Chen, X. He, B. B. Xu and G. Wu, *Nano Lett.*, 2025, **25**, 4485–4493.
4 S. De, J. Florentino, G. Pathiraja, B. Raj Gautam and B. Prasad Bastakoti, *J. Mater. Chem. A*, 2025, **4**, 11300–11313.
5 K. S. Ahmad, S. B. Jaffri, B. Makawana, R. K. Gupta, G. A. Ashraf and Y. S. Usmani, *Ceram. Int.*, 2025, **51**, 11297–11308.
6 K. K. S, K. Kalawat, P. Kour, S. Kour and A. L. Sharma, *Mater. Res. Bull.*, 2025, **184**, 113270.
7 K. Moorthi, M. Padaki and S. Mohan, *Langmuir*, 2025, **41**, 3922–3937.
8 S. Liu, H. Zhang, X. Peng, J. Chen, L. Kang, X. Yin, Y. Yusuke and B. Ding, *ACS Nano*, 2025, **14**, 13591–13636.
9 Q. Zhao, T. Zhao, Y. Han, T. Jiang, J. Zhang, R. Feng and X. Li, *Langmuir*, 2025, **41**, 4702–4713.
10 G. Dhanasekaran, N. Parthiban, T. Keerthana, R. Gopal, S. Sangaraju, S. Chakrabortty and E. Thangavel, *Mater. Sci. Eng., B*, 2025, **313**, 117975.
11 Y. Zhuo, E. Prestat, I. A. Kinloch and M. A. Bissett, *ACS Appl. Energy Mater.*, 2022, **5**, 61–70.
12 S. Irfan, M. Aalim, M. H. Flaifel, I. Nazir, M. A. Shah, M. Q. Lone, A. Firdous, A. H. Pandith and G. N. Dar, *J. Energy Storage*, 2025, **106**, 114788.

13 N. Iqbal, U. Ghani, A. Aboalhassan, Y. Liu, Z. Wang and T. Li, *ACS Appl. Nano Mater.*, 2024, **7**, 12273–12279.
14 N. Choudhary, C. Li, H.-S. Chung, J. Moore, J. Thomas and Y. Jung, *ACS Nano*, 2016, **10**, 10726–10735.
15 Q. Wang, S. Wang, J. Li, L. Ruan, N. Wei, L. Huang, Z. Dong, Q. Cheng, Y. Xiong and W. Zeng, *Adv. Electron. Mater.*, 2020, **6**, 2000388.
16 J. Tang, X. Huang, T. Lin, T. Qiu, H. Huang, X. Zhu, Q. Gu, B. Luo and L. Wang, *Energy Storage Mater.*, 2020, **26**, 550–559.
17 Y. Qian, F. Zhang, X. Luo, Y. Zhong, D. J. Kang and Y. Hu, *Small*, 2024, **20**, 2310526.
18 T. T. Mishra, M. Chakraborty, J. N. Behera and D. Roy, *Energy Fuels*, 2024, **38**, 9186–9217.
19 S. Palchoudhury, K. Ramasamy, J. Han, P. Chen and A. Gupta, *Nanoscale Adv.*, 2023, **5**, 2724–2742.
20 Y. Zhang, W. Feng, M. Ma, N. Zhang, J. Ru, X. Wang, Y. Zhang and X. Zhu, *Surf. Interfaces*, 2024, **48**, 104373.
21 W.-J. Zhang and K.-J. Huang, *Inorg. Chem. Front.*, 2017, **4**, 1602–1620.
22 M. Cen, R. Yan, X. Luo, H. Liu, B. Chen, S. Zhang, W. Peng, Y. Li, Q. Zhang and X. Fan, *Nano Lett.*, 2025, **25**, 1984–1993.
23 P. S. Kiran, K. V. Kumar, N. Pandit, S. Indupuri, R. Kumar, V. V. Wagh, A. Islam and A. K. Keshri, *Adv. Funct. Mater.*, 2024, **34**, 2316266.
24 H. Li, Z. Yin, Q. He, H. Li, X. Huang, G. Lu, D. W. H. Fam, A. I. Y. Tok, Q. Zhang and H. Zhang, *Small*, 2012, **8**, 63–67.
25 Y. Zhang, R. Zhang, Y. Guo, Y. Li and K. Li, *J. Alloys Compd.*, 2024, **998**, 174916.
26 Z. Zeng, Z. Yin, X. Huang, H. Li, Q. He, G. Lu, F. Boey and H. Zhang, *Angew. Chem.*, 2011, **123**, 11289–11293.
27 S. Wu, C. Huang, G. Aivazian, J. S. Ross, D. H. Cobden and X. Xu, *ACS Nano*, 2013, **7**, 2768–2772.
28 Y. Zhan, Z. Liu, S. Najmaei, P. M. Ajayan and J. Lou, *Small*, 2012, **8**, 966–971.
29 X. Zhang, X. Huang, M. Xue, X. Ye, W. Lei, H. Tang and C. Li, *Mater. Lett.*, 2015, **148**, 67–70.
30 S. Mallick, S. Majumder, P. Maiti, K. Kesavan, A. Rahman and A. Rath, *Small*, 2024, **20**, 2403225.
31 Q. Jia, Y. Zhang, J. Xu, Y. Zhao, Q. Wang, S. Rui, L. Meng, H. Li, S. Lu and Y. Zhang, *J. Energy Storage*, 2025, **110**, 115242.
32 C. K. Chua, A. H. Loo and M. Pumera, *Chem.–Eur. J.*, 2016, **22**, 14336–14341.
33 C. Yan, M. Xu, J. Li, H. Wang and P. Huo, *Fuel*, 2024, **378**, 132921.
34 X. Yan, Q.-Y. Huang, T.-Y. Yang, D.-Y. Yu, H. Yin, C.-Y. Wang, Z.-H. Ge, Y.-X. Zhang and H.-J. Pan, *J. Mater. Chem. C*, 2025, **13**, 6085–6094.
35 S. Mohapatra, H. T. Das, B. Chandra Tripathy and N. Das, *ACS Appl. Nano Mater.*, 2024, **7**, 3249–3259.
36 B. A. Ali, O. I. Metwalli, A. S. G. Khalil and N. K. Allam, *ACS Omega*, 2018, **3**, 16301–16308.
37 D. G. S. Quattrociocchi, M. V. M. Meuser, G. B. Ferreira, J. W. De M. Carneiro, S. R. Stoyanov and L. M. Da Costa, *J. Mol. Model.*, 2017, **23**, 60.
38 X. Zhang, Y. Guo, J. Tian, B. Sun, Z. Liang, X. Xu and H. Cui, *Appl. Catal., B*, 2018, **232**, 355–364.
39 M. A. del Valle, P. Cury and R. Schrebler, *Electrochim. Acta*, 2002, **48**, 397–405.
40 Z. Wu, C. Pan, Z. Yao, Q. Zhao and Y. Xie, *Cryst. Growth Des.*, 2006, **6**, 1717–1719.
41 H. Li, H. Li, Z. Wu, L. Zhu, C. Li, S. Lin, X. Zhu and Y. Sun, *J. Mater. Sci. Technol.*, 2022, **123**, 34–40.
42 L. Kang, S. Liu, Q. Zhang, J. Zou, J. Ai, D. Qiao, W. Zhong, Y. Liu, S. C. Jun, Y. Yamauchi and J. Zhang, *ACS Nano*, 2024, **18**, 2149–2161.
43 T. Xiang, Q. Fang, H. Xie, C. Wu, C. Wang, Y. Zhou, D. Liu, S. Chen, A. Khalil, S. Tao, Q. Liu and L. Song, *Nanoscale*, 2017, **9**, 6975–6983.
44 H. Li, Q. Zhang, C. C. R. Yap, B. K. Tay, T. H. T. Edwin, A. Olivier and D. Baillargeat, *Adv. Funct. Mater.*, 2012, **22**, 1385–1390.
45 S. Cortijo-Campos, P. Kung, C. Prieto and A. de Andrés, *J. Phys. Chem. C*, 2021, **125**, 23904–23910.
46 S. Das, G. Swain and K. Parida, *Mater. Chem. Front.*, 2021, **5**, 2143–2172.
47 B. R. Carvalho, Y. Wang, S. Mignuzzi, D. Roy, M. Terrones, C. Fantini, V. H. Crespi, L. M. Malard and M. A. Pimenta, *Nat. Commun.*, 2017, **8**, 14670.
48 R. Thangappan, S. Kalaiselvam, A. Elayaperumal, R. Jayavel, M. Arivanandhan, R. Karthikeyan and Y. Hayakawa, *Dalton Trans.*, 2016, **45**, 2637–2646.
49 M. Mohan, N. P. Shetti and T. M. Aminabhavi, *J. Energy Storage*, 2023, **58**, 106321.
50 A. Das, A. Maitra, A. Mondal, A. De, P. Maity and B. B. Khatua, *J. Energy Storage*, 2024, **92**, 112293.
51 N. B. Velhal, N. C. Maile, C. Paeng, H. Lee, T. Kim, J. Kim and C. Yim, *J. Energy Storage*, 2024, **90**, 111764.
52 C. Zhang, X. Cai, Y. Qian, H. Jiang, L. Zhou, B. Li, L. Lai, Z. Shen and W. Huang, *Adv. Sci.*, 2018, **5**, 1700375.
53 S. Sundriyal, V. Shrivastav, H. Kaur, S. Mishra and A. Deep, *ACS Omega*, 2018, **3**, 17348–17358.
54 H. Xu, Y. Zhang, F. Liu, Z. Yang, J. Xu and J. Liu, *ACS Appl. Nano Mater.*, 2024, **7**, 21340–21350.
55 H. Li, Z. Wei, X. Yuan, Y. Zhao, Q. Jia, Y. Li, D. Ma, B. Li, Y. Zhang and X. Zhu, *J. Power Sources*, 2024, **608**, 234648.
56 K. P. Shwetha, M. K. Sudha Kamath, C. K. Rastogi, Y. Athreya, S. Sudhakaran and C. Manjunatha, *J. Energy Storage*, 2024, **97**, 112699.

